Journal of Applied Polymer Science

Thermal and mechanical properties of nanocomposites based on a PLLA-*b*-PEO-*b*-PLLA triblock copolymer and nanohydroxyapatite

Lívia M. D. Loiola,[1] Laura A. Fasce,[2] Laura C. E. da Silva,[1] Maria C. Gonçalves,[1] Patricia M. Frontini,[2] Maria I. Felisberti[1]

[1]Institute of Chemistry, University of Campinas (UNICAMP), P.O. Box 6154, 13083-970, Campinas, São Paulo, Brazil

[2]Universidad Nacional De Mar Del Plata, Instituto De Investigaciones En Ciencia Y Tecnología De Materiales, INTEMA, J.B. Justo 4302 - B7608 FDQ - Mar Del Plata, Argentina

Correspondence to: M. I. Felisberti (E-mail: misabel@iqm.unicamp.br)

ABSTRACT: Composites which combine biocompatible polymers and hydroxyapatite are unique materials with regards to their mechanical properties and bioactivity in the development of temporary bone-fixation devices. Nanocomposites based on a biocompatible and amphiphilic triblock copolymer of poly(L-lactide) (PLLA) and poly(ethylene oxide) (PEO) —PLLA-*b*-PEO-*b*-PLLA— and neat (nHAp) or PEO-modified (nHAp@PEO) hydroxyapatite nanoparticles were prepared by dispersion in benzene solutions, followed by freeze-drying and injection moulding processes. The morphology of the copolymers of a PEO block dispersed throughout a PLLA matrix was not changed with addition of the nanofillers. The nHAp particles were spherical and, after modification, the nHAp@PEO nanoparticles were partially agglomerated. In the nanocomposites, these particles characteristics remained unchanged, and the nHAp particles and nHAp@PEO agglomerates were uniformly dispersed through the copolymer matrix. These particles acted as nucleating agents, with nHAp@PEO being more efficient. The incorporation of nHAp increased both the reduced elastic modulus (~22%) and the indentation hardness (~15%) in comparison to the copolymer matrix, as determined by nanoindentation tests, while nHAp@PEO addition resulted in lower increments of these mechanical parameters. The incorporation of untreated nHAp was, therefore, more beneficial with regards to the mechanical properties, since the amphiphilic PLLA-*b*-PEO-*b*-PLLA matrix was already efficient for nHAp nanoparticles dispersion. © 2016 Wiley Periodicals, Inc. J. Appl. Polym. Sci. **2016**, *133*, 44187.

KEYWORDS: mechanical properties; morphology; nanocomposites; thermal properties; triblock copolymer

Received 25 May 2016; accepted 17 July 2016

DOI: 10.1002/app.44187

INTRODUCTION

Bioabsorbable polymeric materials, such as the aliphatic polyesters poly(lactide), poly(ε-caprolactone), and poly(glycolide), have been progressively applied in the manufacture of medical devices, including tissue engineering scaffolds,[1–4] controlled drug delivery systems,[5–7] and implantable devices[8,9] because of the hydrolytic and enzymatic degradation under biological conditions to non-toxic products.[10]

Poly(L-lactide) (PLLA) is one of the most applied polyesters in biomedical field. It is used to produce biodegradable devices such as surgical sutures[11] and scaffolds for temporary bone fixation[12,13] due to its feasible *in vivo* degradation. However, its bioabsorption can be limited due to its hydrophobic surface and high crystallinity, which are, respectively, responsible for limiting the cell adhesion and mechanical behavior.[14]

Copolymerization of PLLA with hydrophilic blocks, such as poly(ethylene oxide) (PEO), is a useful method for tailoring its surface and bulk physical–chemical characteristics. The hydrophilic nature of a PEO block improves the adhesion of the PLLA with synthetic ceramic materials based on calcium phosphates, such as nanohydroxyapatite (nHAp, $Ca_{10}(PO_4)_6(OH)_2$) and beta-tricalcium phosphates (β-TCP).[15] These inorganic particles have been applied as dispersed phases in polymeric biocomposites[16,17] due to their similarity to the mineral phase of bone in terms of composition and bioactivity.[18]

Hydroxyapatite dispersion in a polymeric matrix enhances the thermal and mechanical properties of the overall material.[6,7] In addition, nHAp neutralizes the acid degradation products of PLLA-based copolymers due to the release of basic ions in the implantation site, which minimizes the inflammatory response[19] and improves osteoblast adhesion, proliferation and differentiation.[14,20]

Additional Supporting Information may be found in the online version of this article.

Nevertheless, the dispersion of nHAp particles in a polymeric matrix is a crucial factor for the performance of these composites.[21,22] The surface modification of nHAp with a copolymer component, such as low molar mass PEO or PLLA, in the case of PLLA/PEO copolymers, has been described in the literature as a successful strategy to avoid particles agglomeration by favoring nHAp/copolymer interactions.[23–25]

To enhance the dispersion of nHAp particles into a poly(ε-caprolactone)-poly(ethylene oxide)-poly(ε–caprolactone) (PCEC) polymeric matrix, Fu *et al.* coated nHAp with PEO and the resulting modified particles were applied as fillers in composite membranes at 0–40 wt % of nHAp@PEO. The composite membranes were more hydrophilic than neat PCEC, and consequently, the degradation rate increased with increasing particle content. The tensile strength and elongation decreased with an increase in the nHAp@PEO content while the Young's modulus increased in comparison to neat copolymer.[26] However, the authors did not compare the performance of composites with nHAp@PEO and neat nHAp particles as fillers.

Fibrous composites were fabricated by electrospinning from dispersions of nHAp and nHAp@PEO into PLLA homopolymer solutions in $CHCl_3$/DMF (7/3 v/v). The morphology of the PLLA/nHAp@PEO fibres showed a smooth fibre surface, which was attributed to nHAp@PEO being uniformly distributed in the PLLA matrix, in comparison to PLLA/nHAp fibres that presented defects due to particle agglomeration.[23]

The amphiphilic triblock copolymer, PLLA-*b*-PEO-*b*-PLLA, was reported by Kutikov and Song to be able to improve the stability of hydroxyapatite suspensions in organic solvents, in comparison to the PLLA homopolymer.[27] Once the hydrophilic PEO block enhanced the particle adhesion to the overall polymer, fibrous composites with more uniform fibre dimensions and better hydroxyapatite distribution were prepared by electrospinning.[27]

PLLA-*b*-PEO-*b*-PLLA amphiphilic triblock copolymers present a flexible and hydrophilic PEO middle block, and hard and hydrophobic PLLA end blocks. The non-cytotoxic character of PLLA-*b*-PEO-*b*-PLLA was previously demonstrated thorough PicoGreen® assays, indicating that these copolymers are biocompatible candidates for tissue engineering applications.[28] No individual polymer, however, can meet all the requirements for the design of temporary devices. Nanocomposites consisting of a polymer matrix and nHAp can offer an improved set of properties in comparison to their individual components, which make them suitable candidates for bone tissue engineering regeneration.[29] Additionally, nano-sized particles provide substantially higher interfacial area for load transfer when incorporated into a polymeric composite matrix compared to their micro-sized counterparts.[30]

The current study is aimed at the development of nanocomposites based on a PLLA-*b*-PEO-*b*-PLLA copolymer matrix and hydroxyapatite nanoparticles, and the investigation of the influence of the nanofiller, nHAp, and also of the filler with a PEO capping (nHAp@PEO), on the morphology and overall thermal and mechanical properties. The applied strategies were: (i) synthesis of the PLLA-*b*-PEO-*b*-PLLA copolymer; (ii) surface modification of nHAp using low molar mass PEO; (iii) nanocomposite preparation by dispersion of nHAp or nHAp@PEO particles in a copolymer benzene solution, followed by freeze-drying; and (iv) preparation of micro-samples by micro-injection moulding for material characterization. The nanocomposites were characterized by means of thermal analyses, nano-indentation experiments, and morphology.

EXPERIMENTAL

Materials

L-lactide (LLA, 144 g/mol, Sigma-Aldrich) and poly(ethylene oxide) (PEO_{29}, Sigma-Aldrich, $M_n = 29$ kg/mol, $M_w/M_n = 1.2$ and PEO_8, Fluka, $M_n = 8$ kg/mol, $M_w/M_n = 1.1$) were lyophilized to remove residual water prior to use. The catalyst, $Sn(Oct)_2$, and the poly(L-lactide) ($PLLA_{85}$, Sigma-Aldrich, $M_n =$ 85 kg/mol, $M_w/M_n = 2.3$) were used as received. Hydroxyapatite nanopowder (nHAp, $Ca_5(OH)(PO_4)_3$, 502.31 g/mol, Sigma-Aldrich) was dried under vacuum at 100 °C for 3 h. The solvents, *N*,*N*-dimethyformamide (DMF, PA, Vetec), ethanol (PA, Synth), and benzene (PA ACS, Êxodo Científica), were used as received, and toluene (PA ACS, Synth) was used after being dehydrated with a 5 Å molecular sieve (Sigma-Aldrich).

Copolymer Synthesis

The copolymer was synthesized by ROP in anhydrous toluene solutions ($m_{copolymer}$:$V_{toluene} = 1{:}10$) under an argon atmosphere. Appropriate amounts of $Sn(Oct)_2$ and PEO_{29} macroinitiator ($n_{catalyst}$:$n_{macroinitiator} = 2{:}1$, method "A" described by Trinca and Felisberti[31]) were initially added to a round-bottom flask, and the mixture was kept under toluene reflux with continuous stirring for 1 h. After this pre-activation step, LLA was added, and the reaction solution was kept under reflux for 44 h. The copolymer was precipitated in cold ethyl ether ($V_{reaction\ solution}$:$V_{ether} = 1{:}10$), filtered, and dried under vacuum at 40 °C for 48 h. The yield was 91%.

Hydroxyapatite Nanoparticle Modification

nHAp particles were functionalized with PEO with $M_n = 8$ kg/mol. PEO_8 was added to a nHAp suspension in DMF (m_{nHAp}:$V_{DMF} = 0.04{:}10$ and m_{nHAp}:$m_{PEO} = 1{:}1$), and the mixture was stirred for 48 h, then centrifuged at 13,000 rpm for 60 min. The supernatant was removed and the material was washed twice with ethanol to remove the excess of PEO_8. The PEO_8 functionalized nHAp (nHAp@PEO) was dried under vacuum at 40 °C for 48 h.[26]

Preparation of Nanocomposites and Micro-Injection Moulded Samples

Copolymer 15 wt % benzene solutions were prepared, and nHAp or nHAp@PEO were dispersed by sonication for 4 h to form viscous suspensions ($m_{particle}$:$m_{copolymer} = 1{:}10$). The suspensions were vigorously stirred and immediately freeze-dried for 24 h. These pre-mixtures were injection moulded to obtain specimens for characterization using an injection moulding machine, DSM Xplore, under a pressure of 6 bar and at heater and mould temperatures of 180 and 40 °C, respectively. Rectangular specimens of 8.0 × 5.0 × 1.3 mm^3 were prepared for dynamic mechanical analysis (DMA), cylindrical specimens with

Table I. Molecular Characteristics of PEO, PLLA, and the PLLA-*b*-PEO-*b*-PLLA Copolymer

		Final composition			
Polymer	n_{LLA}/n^{a}_{EO}	PEO:PLLA[a] mass ratio	M_n [a] (g/mol)	M_n [b] (g/mol)	M_w/M_n [b]
PEO_8	—	100:0	8000	12000	1.1
PEO_{29}	—	100:0	29000	40000	1.2
$PLLA_{85}$	—	0:100	—	85000	2.3
PLLA-*b*-PEO-*b*-PLLA	0.9	26:74	115000	43000	1.6

Determined by [a]^{1}H NMR and [b]GPC.

diameters of 5.0 mm, and heights of 3.5 mm were moulded for nanoindentation tests, and also, discs of 1 mm in height were obtained for differential scanning calorimetry (DSC). The pictures of the specimens are shown in Figure S1 of the Supporting Information. The same injection moulding conditions were adopted for the copolymer and PLLA 85 kg/mol samples, while in the case of PEO 29 kg/mol, the injection moulding was performed under a 4 bar pressure and at 75 °C, with the mould kept at 30 °C.

Characterization Methods

Copolymer Structure. ^{1}H NMR spectra of deuterated chloroform (chloroform-*d*, 99.8% containing 0.05% tetramethysilane (TMS), Cambridge Isotope) copolymer solutions (15 mg in 0.7 mL of chloroform-*d*) were recorded at room temperature on an Avance AC/P 400 MHz spectrometer (Bruker). Chemical shifts (δ) in ppm were referenced to the TMS internal standard.

The number average molar masses (M_n, Table I) of PEO_8 and PEO_{29} were determined using the method described by Kricheldorf and Meier-Haack,[32] which consists of determining the molar ratio between the hydroxyl end-groups and main-chain protons (—CH_2— at 3.6 ppm) by ^{1}H NMR spectroscopy after the quantitative reaction between trifluoroacetic anhydride and the —OH end-groups (—CH_2—OCOCF_3 shifted to 4.5 ppm in esterified PEO).

The number-average molar mass (M_n) and block mass ratio (PEO:PLLA) of the PLLA-*b*-PEO-*b*-PLLA copolymer (Table I) were calculated from the signal area ratios from the methine protons of the PLLA lactyl units (—CH(CH_3)— at 5.18 ppm) and the methylene protons of the PEO ethylene oxide groups (—CH_2— at 3.6 ppm) in the ^{1}H NMR spectrum (Figure S2 Supporting Information), considering the previously calculated M_n for PEO_{29}.[33–36]

The number-average molar mass (M_n), weight-average molar mass (M_w), and polydispersity index (M_w/M_n) of the PLLA-*b*-PEO-*b*-PLLA copolymer and homopolymers (Table I) were determined by GPC performed on a Viscotek GPCmax VE2001 instrument equipped with a Viscotek VE3580 refractive index and Viscotek UV2500 detectors and three Shodex KF-806M columns. The column system was kept at 40 °C and tetrahydrofuran was used as an eluent at a flow rate of 1 mL/min. Molar masses were calculated relative to PS standards (Viscotek, molar masses from 1050 to 3,800,000 g/mol). The chromatograms of the PLLA-*b*-PEO-*b*-PLLA copolymer directly after the synthesis, and also after processing, are depicted in Figure S3 of the Supporting Information.

Nanoparticle Structure. X-ray diffraction (XRD) measurements for the nHAp and nHAp@PEO particles were carried out using a Shimadzu XRD-7000. The radiation source (Cu-Kα X-ray, $\lambda = 0.1542$ nm) was operated at 40.0 kV and 30.0 mA, with a scanning angle ranging from 5 to 50° and a scanning rate of 2° min^{-1}.

The crystal size was calculated according to the Debye–Scherrer equation[37]:

$$D_{hkl} = {K\lambda}/{\beta_{1/2}} \cos\theta \quad (1)$$

where D_{hkl} is the average crystallite size in the direction of (*hkl*) diffraction planes, K is a numerical factor referred to the crystallite-shape factor ($K = 0.89$ for the hydroxyapatite crystal habit), λ is the wavelength of the Cu-Kα radiation ($\lambda = 1.542$ Å) and θ is the Bragg angle of the characteristic XRD peak. The crystal sizes along (002) and (310) diffraction planes correspond to the length and width of the nHAp crystallite, respectively.[38]

The amount of PEO_8 coated on the nHAp@PEO particles was determined by thermogravimetry performed on a TA Instruments TGA 2950 under an argon atmosphere (with a 100 mL/min flow rate) at a 10 °C/min heating rate from 30 to 800 °C.

Suspensions of nHAp and nHAp@PEO in ethanol (1.5 mg/mL) were prepared and dripped on top of a carbon coated copper grid and left to dry. The samples were analyzed in a Carl Zeiss Libra 120 transmission electron microscope (TEM; 120 kV) equipped with an in-column OMEGA energy filter spectrometer and an Olympus 14 bits CCD camera with 1376 × 1032 resolution.

Homopolymers, Copolymer, and Nanocomposites Characterization. DSC experiments were performed on a TA Instruments Q2000 operating at a 20 °C/min rate. Samples were heated from −80 to 200 °C (first heating), kept at 200 °C for 2 min, cooled from 200 to −100 °C (cooling), kept at −100 °C for 10 min, and then heated again from −100 to 200 °C (second heating). DSC curves were normalized with respect to sample mass (approximately 10 mg).

The crystallinity degree (X_c) of PLLA was calculated according to the equation:

$$X_c = {}^{\Delta H_m}\Big/ \left(w \times \Delta H_{m,100}\%\right) \quad (2)$$

where ΔH_m is the melting enthalpy related to the endothermic peak, $\Delta H_{m,100\%}$ is the melting enthalpy for 100% crystalline PLLA, taken as 93 J/g,[14] and w is the mass fraction of PLLA in the samples.

DMA experiments were performed on a DMTA V from Rheometric Scientific® with a 0.01% strain at a 1 Hz frequency. Samples were loaded onto a tension fixture with a 6-mm gap and equilibrated at −100 °C. The dynamic mechanical properties were recorded during heating at 2 °C/min from −100 to 200 °C.

Cross-sections of micro-injection moulded specimens were obtained by cryogenic fracture for scanning electron microscopy (SEM) analysis. Samples were Pt sputter coated in a MD 020 (Bal-Tec) sputter coater. SEM inspection was carried out in a JSM-6360 (JEOL) SEM, operating at an accelerating voltage of 10 kV.

Approximately 35 nm thick ultrathin sections were cut from injection moulded specimens in a Leica EM FC6 cryo-ultramicrotome using a diamond knife at −100 °C to prepare TEM samples. TEM investigations were carried out on the Carl Zeiss Libra 120 TEM.

Nanoindentation tests were performed in a Triboindenter (Hysitron) at 23 °C and 50% of relative humidity using a diamond Berkovich tip. Two sets of tests were carried out and for each set and sample, at least 20 indentations were performed at different surface locations. In all cases, displacement data were corrected by thermal drift effect following the procedure recommended by Hysitron. To obtain representative properties of the bulk materials, large penetration depths were used, assuring that the deformation volumes were significantly larger than the size of the morphological domains of the nanocomposites.

Quasi-static mechanical properties (E and H) were evaluated from indentation experiments performed at a maximum load of 3 mN and at loading/unloading rates of 300 μN/s. A holding time of 15 s was applied at maximum load to minimize creep effects in the unloading curve. Under these conditions, the unloading was assumed to be elastic and the Oliver-Pharr approach[39] was applied (Supporting Information eq. S1-S3).

The viscoelastic response of the materials, was evaluated from tests carried out by applying a fast loading stage at 3000 μN/s to limit relaxation phenomena and holding the load at 3000 μN during 50 s. Displacement data recorded during the holding stage (h) were interpreted using the indentation creep phenomenological model proposed by Beake[40,41] (Supporting Information eq. S4).

Scanning probe microscopy (SPM) images of the impressions remaining on the sample surfaces, after testing, were obtained using the SPM module of the Triboindenter.

RESULTS AND DISCUSSION

Copolymer Synthesis and Characterization

Table I presents the composition of the polymers, expressed as the LLA and EO units molar ratio (n_{LLA}/n_{EO}) and block mass ratio (PEO:PLLA), and polydispersity indexes (M_w/M_n), arising from ^{1}H NMR and GPC analyses (Figures S2 and S3 Supporting Information, respectively).

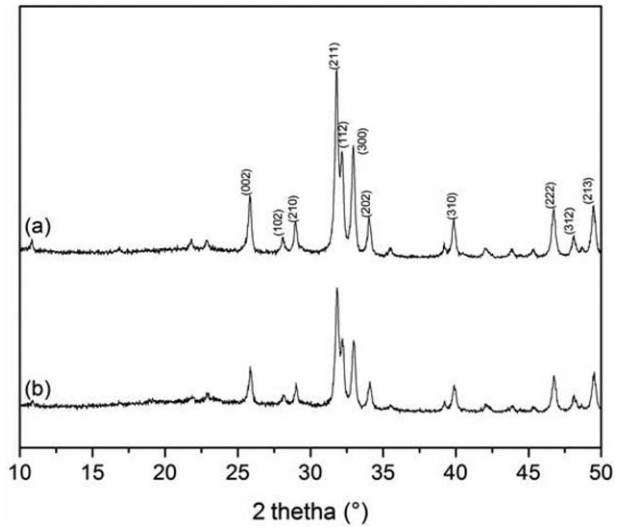

Figure 1. XRD patterns of (a) nanohydroxyapatite (nHAp) and (b) nanohydroapatite modified with PEO (nHAp@PEO). The peaks assignment was done according to ref. 42.

As mentioned in the Experimental section, the copolymer was subjected to sonication and to injection moulding from the melting state. A shift in the elution volume from 27.1 to 27.5 mL, and in the polydispersity index (M_w/M_n) from 1.6 to 2.3, was observed, indicating that the processing caused changes in the PLLA-*b*-PEO-*b*-PLLA copolymer molar mass and its distribution. The chromatograms of the PLLA-*b*-PEO-*b*-PLLA copolymer, before and after processing, are depicted in Figure S3 of the Supporting Information.

nHAp and nHAp@PEO Structure Characterization

Figure 1 show the XRD patterns of nHAp and nHAp@PEO. The nHAp diffraction pattern reveals three main peaks at Bragg's diffraction angles of $2\theta = 25.8$, 31.8, and 32.9°, which respectively correspond to the (002), (211), and (300) diffraction planes.[26,43,44] These observations are consistent with the standard XRD pattern for hexagonal nHAp.[42,45] The diffraction peaks of nHAp@PEO appear at the same angles, however they are broader and more diffuse than those of nHAp, due to the presence of PEO_8 capping.

The full widths at half maximum ($\beta_{1/2}$) of XRD peaks at $2\theta = 25.8°$ and 39.9° were respectively used to calculate the length (D_{002}) and width (D_{310}) of the crystallites [eq. (1)]. Hydroxyapatite crystallites presented $D_{002} = 30$ nm and $D_{310} = 32$ nm for nHAp, and $D_{002} = 28$ nm and $D_{310} = 28$ nm for nHAp@PEO.

The thermogravimetric curves of PEO_8, nHAp, and nHAp@PEO (Figure 2) show an initial mass loss for both nHAp and nHAp@PEO of about 0.7% around 220 °C and it is probably due to moisture (Figure 2: inset). After that, no significant mass loss events were observed for nHAp. Hydroxyapatites, as hydrated calcium phosphate materials, begin to gradually

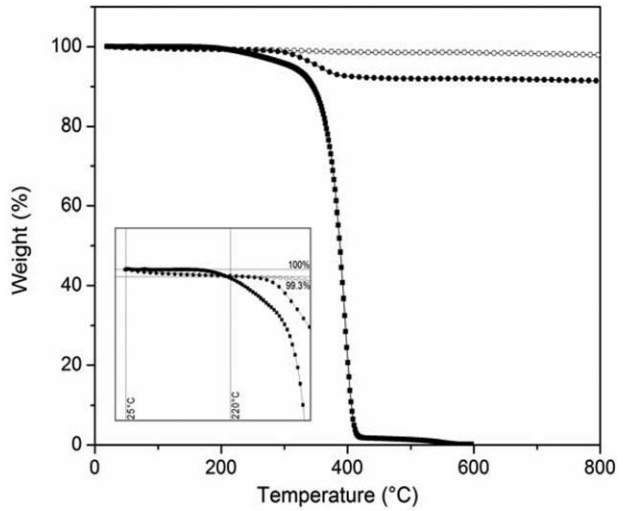

Figure 2. Thermogravimetric curves of (■) PEO_8, (○) nHAp, and (•) nHAp@PEO particles under argon atmosphere. The inset highlights the initial mass loss from nHAp and nHAp@PEO.

dehydroxylate at around 800 °C to form oxyhydroxyapatite.[24] From the registered nHAp@PEO thermogravimetric data up to 500 °C, a thermal degradation event starting around 360 °C was associated to PEO_8 degradation, and thus, it was concluded that 7 wt % PEO_8 was adsorbed on the nHAp surface.[25] Yamini *et al.* synthesized nHAp particles and PEO functionalized nHAp (nHAp@PEO). Raman spectral measurements have been performed and the active vibrational modes of PEO were highly influenced by the electrostatic interaction between the two materials, evidencing the non-specific adsorption of PEO on the nHAp surface.[25]

nHAp and nHAp@PEO particles are predominantly spherical with diameters of 78 ± 39 and 79 ± 37 nm, respectively, as determined by TEM (the diameter distribution curves of the particles are shown in Figure S4 Supporting Information).

TEM bright field images of nHAp and nHAp@PEO are shown in Figure 3(a–c), respectively. TEM bright field images show a darker region, which is related to the denser phase, that is, to the nanohydroxyapatite particles in both nHAp and nHAp@-PEO. Alternatively, the grey region around the nHAp@PEO nanoparticles is thought to be the 5 ± 2 nm thick PEO capping. The chemical composition of the nanoparticle capping was investigated through electron energy loss spectroscopy using a 10 eV energy slit. The carbon and calcium maps are shown in Figure 3(d,e), respectively. These maps reveal that the ring formed by the lighter contrast in Figure 3(c) is mainly composed of carbon, while the particle itself is mainly composed of calcium, which confirms the PEO layer adsorbed on the nanohydroxyapatite surface. The observed TEM particles dimensions are higher than the corresponding crystallite size (i.e., 28–30 nm), which is expected due to the fact that these nanoparticles are polycrystalline.[46]

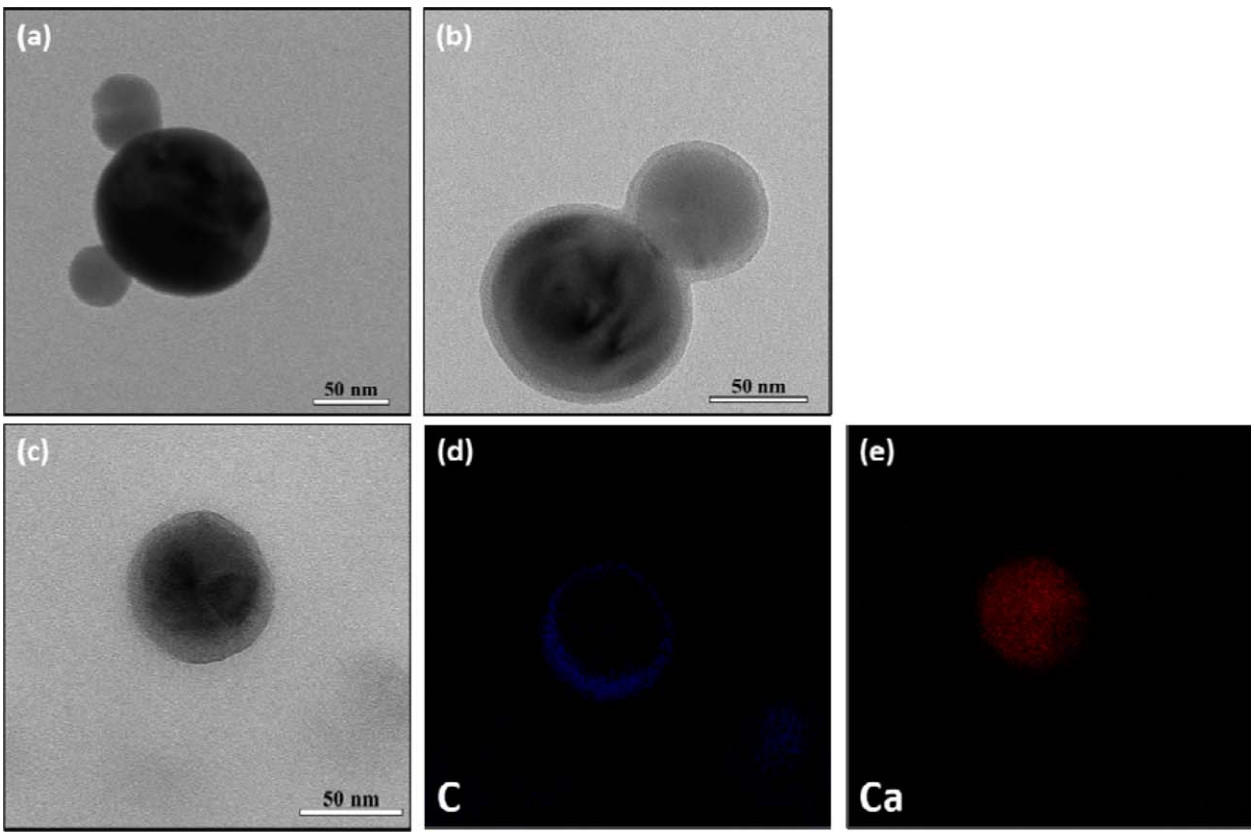

Figure 3. TEM bright field micrograph of (a) nHAp, (b) and (c) nHAp@PEO and its (d) carbon (in blue) and (e) calcium (in red) maps. [Color figure can be viewed in the online issue, which is available at wileyonlinelibrary.com.]

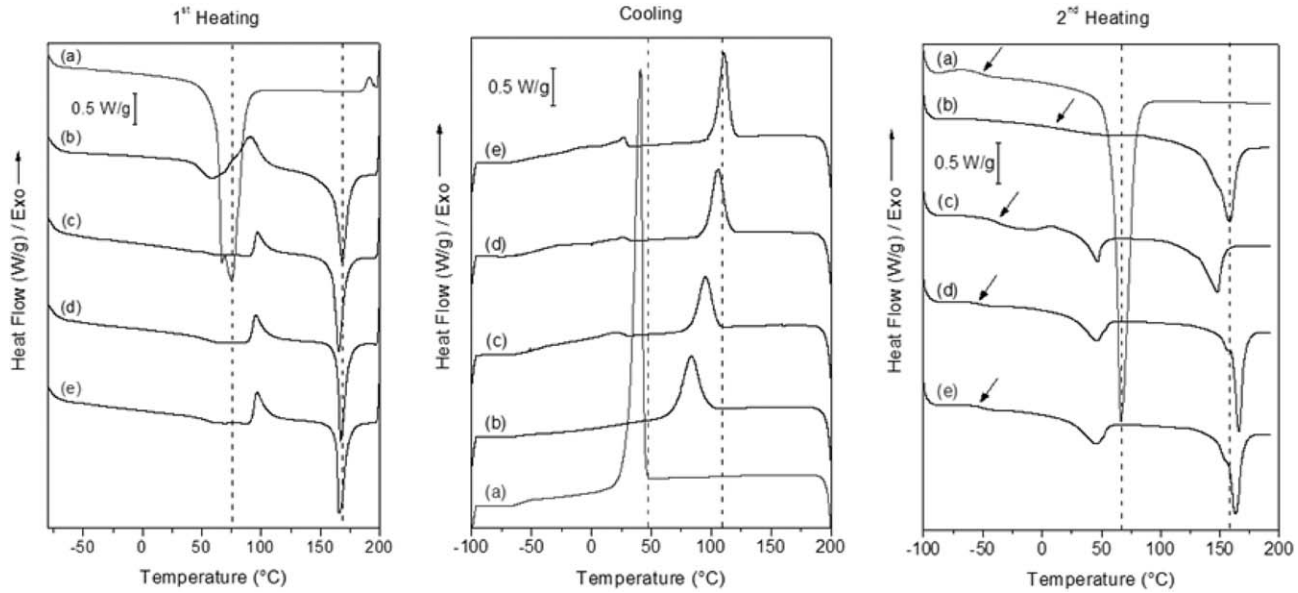

Figure 4. DSC curves for first heating, cooling and second heating at 20 °C/min of (a) PEO 29 kg/mol, (b) PLLA 85 kg/mol, (c) PLLA-*b*-PEO-*b*-PLLA copolymer, nanocomposites of (d) nHAp, and (e) nHAp@PEO. The vertical lines mark the melting peak temperatures of the PEO and PLLA homopolymers in the heating curves, while in the cooling curves, the crystallization onset temperature of the homopolymers is highlighted. The arrows point out the glass transitions of the materials.

The superficial modification of the hydroxyapatite with PEO was able to improve the nHAp@PEO suspension stability in the copolymer solutions (in benzene and in ethanol), in comparison to neat nHAp suspensions. This effect may be attributed to the steric repulsion originating from adsorbed PEO on the nHAp@-PEO surfaces.[47] After solvent removal, particle aggregation occurs, as depicted by TEM bright field images (Supporting Information S4), and this effect is more pronounced in nHAp@PEO nanoparticles. Similar results have been reported by Cheng *et al.* for nHAp@PEO/PLLA scaffolds prepared from homogeneous suspensions in $CHCl_3$/DMF. The aggregation resulted from the affinity between nHAp@PEO particles.[23]

Nanocomposites Characterization

The thermal transitions of the homopolymers, copolymer and nanocomposites, determined using DSC (Figure 4), are summarized in Table II. For $PLLA_{85}$, copolymer and nanocomposites, a glass transition in the first heating occurred at approximately $T_g = 50\,°C$. These polymeric systems crystallized and melted during the first heating, as depicted, respectively, by exothermic and endothermic peaks with temperature of T_c at 95 °C and mininum temperature of T_m at 166 °C. The described T_g and the subsequent crystallization and melting events of the first heating refer to the PLLA phase. PEO_{29} melting during the first heating is depicted by an endothermic peak with $T_m = 75\,°C$. There is no evidence of the presence of crystalline PEO phase in the injection moulded copolymer and nanocomposites.

In the cooling curves, PEO_{29} and $PLLA_{85}$ homopolymers crystallization occurred at $T_c = 41\,°C$ and 83 °C, respectively. All the other samples displayed an exothermic and intense peak at approximately 100 °C, referring to PLLA crystallization and a less intense peak assigned to PEO phase crystallization at approximately 20 °C.[48]

The glass transition in the second heating occurred at $T_g = -40\,°C$ for the copolymer and at $T_g = -50\,°C$ for the nanocomposites, and is associated with the PEO phase. The two endothermic peaks at approximately 45 and 160 °C in the second heating curves came from the melting of the crystalline phases of PEO and PLLA, respectively. The PEO_{29} and $PLLA_{85}$ homopolymers melted at $T_{m,PEO} = 66\,°C$ and $T_{m,\ PLLA} = 158\,°C$ in the second heating.

The crystallization temperature for PLLA blocks in the copolymer during cooling is higher for the nanocomposites than that for the pure copolymer, which suggests that the dispersed inorganic particles act as the centre of nucleation and induce earlier formation of PLLA nuclei.[49] Compared with the nHAp nanocomposite, the higher crystallization temperature of the nHAp@PEO nanocomposite indicates the more efficient nucleating action of nHAp@PEO compared to nHAp for polymeric segments. The melting peaks of nanocomposites during the second heating shifted to higher temperatures, as compared with the pure copolymer, as a consequence of the higher lamellae thickness. However, the crystallinity degree of PLLA phase was not influenced by the nHAp capping. The effect of the nanoparticles on the crystallization of PEO phase followed the same trend observed for PLLA.

The PLLA mass fraction (w) in the crystallinity degree (X_c) calculation [eq. (2)] was taken as 74 wt % for the copolymer (Table I) and 67 wt % for the nanocomposites. The comparison of X_c values reported in Table II ($X_c = 48$, 58, and 61%, for the copolymer and nanocomposites with nHAp and nHAp@PEO, respectively, taken the ΔH_m from the second heating scans to ensure the same thermal history of crystalline phase formation) shows that inorganic particles cause an increase in the crystallinity degree of the PLLA phase in the nanocomposites.

Table II. Thermal Properties of Homopolymers, PLLA-*b*-PEO-*b*-PLLA Copolymer and Nanocomposites Determined by DSC and DMA, and Mechanical Parameters Determined from Nanoindentation Experiments

		Material				
		$PLLA_{85}$	PLLA-*b*-PEO-*b*-PLLA	nHAp composite	nHAp@PEO composite	PEO_{29}
T_g (°C)	First heating	47	55	50	50	—
	Second heating	23	−39	−51	−50	—
$T_{c\ PLLA}$ (°C)	First heating	91	97	95	96	—
	Cooling	83	95	106	111	—
$\Delta H_{c\ PLLA}$ (J/g)	First heating	25	10	13	15	—
	Cooling	38	28	31	33	—
$T_{c\ PEO}$ (°C)	Cooling	—	19	25	27	41
$\Delta H_{c\ PEO}$ (J/g)	Cooling	—	1.9	2.7	4.0	161
$T_{m\ PEO}$ (°C)	First heating	—	—	—	—	75
	Second heating	—	47	45	44	66
$\Delta H_{m\ PEO}$ (J/g)	First heating	—	—	—	—	186
	Second heating	—	10	14	15	171
$T_{m\ PLLA}$ (°C)	First heating	168	166	167	166	—
	Second heating	158	148	166	163	—
$\Delta H_{m\ PLLA}$ (J/g)	First heating	51	44	39	40	—
	Second heating	51	33	36	38	—
$X_{c\ PLLA}$ (%)	First heating	28	49	42	40	—
	Second heating	55	48	58	61	—
$T_{g\ PEO}$ (°C)	E'' vs. T	—	−42	−52	−43	—
$T_{g\ PLLA}$ (°C)	tan δ vs. T	—	59	63	54	—
E_r (GPa)	Nanoindentation	2.45 (±0.06)	0.74 (±0.01)	0.91 (±0.02)	0.86 (±0.03)	—
H (MPa)		132.9 (±5.0)	34.5 (±0.4)	39.9 (±0.9)	35.5 (±1.8)	—
$A/h(0)$		0.067 (±0.002)	0.065 (±0.001)	0.074 (±0.002)	0.072 (±0.003)	—
B (nm/s)		3.49 (±0.19)	3.76 (±0.23)	3.65 (±0.23)	3.96 (±0.38)	—
$h(0)$ (nm)		883 (±12)	1581 (±15)	1450 (±22)	1547 (±32)	—

The crystallinity degree of the PLLA blocks in the injection moulded copolymer and nanocomposites can be inferred from the first heating data, from the difference of $\Delta H_m - \Delta H_{c,\ PLLA}$ (Table II). The crystallinity degree of the injection moulded materials ($X_c = 49$, 42, and 40%, respectively) showed the opposite trend in comparison to the DSC second heating experiments. However, this opposing trend in the DSC first heating does not contradict the described nucleating capability of the nHAp and nHAp@PEO particles. It reflects the effect of the processing history and also the differences between the thermal conductivity values (k) of the neat copolymer and nanocomposites. In general, semicrystalline polymers present k values around 0.1–0.3 W m^{-1} K^{-1} [50] while apatites have k values around 1.3–2.0 W m^{-1} K^{-1}.[51] After the thermal moulding, the injected materials were allowed to cool down to room temperature, and the higher thermal conductivity of hydroxyapatite nanocomposites implies in a higher cooling rate for nanocomposites, what could contribute to decrease the crystallinity degree in comparison to the neat copolymer. This effect is not observed in the DSC second heating, because all materials were cooled down at a constant rate of 20 °C/min, and the samples masses were small enough to guarantee an efficient heat transfer during the DSC analyses. The reduction of cooling time of composites, in comparison with the polymeric matrix, by the introduction of fillers with high thermal conductivity, and the implication on the polymer crystallization have been reported previously.[52–54]

Figure 5 shows the SEM micrographs of the nanocomposites containing 10 wt % of nHAp [Figure 5(a)] and 10 wt % of nHAp@PEO [Figure 5(b)]. These micrographs show that nHAp particles are uniformly dispersed, while nHAp@PEO particles are more agglomerated. Particle aggregation of nHAp@PEO occurred already during capping, as depicted by TEM bright field images (Supporting Information S4).

TEM images of ultrathin films cut from injection moulded PLLA-*b*-PEO-*b*-PLLA [Figure 6(a)] present a dark and diffuse phase, probably due to PEO middle block phase disperse in the PLLA matrix. This phase is not observed for the nHAp nanocomposite [Figure 6(b)], suggesting that PEO blocks are adsorbed on the nHAp surface.

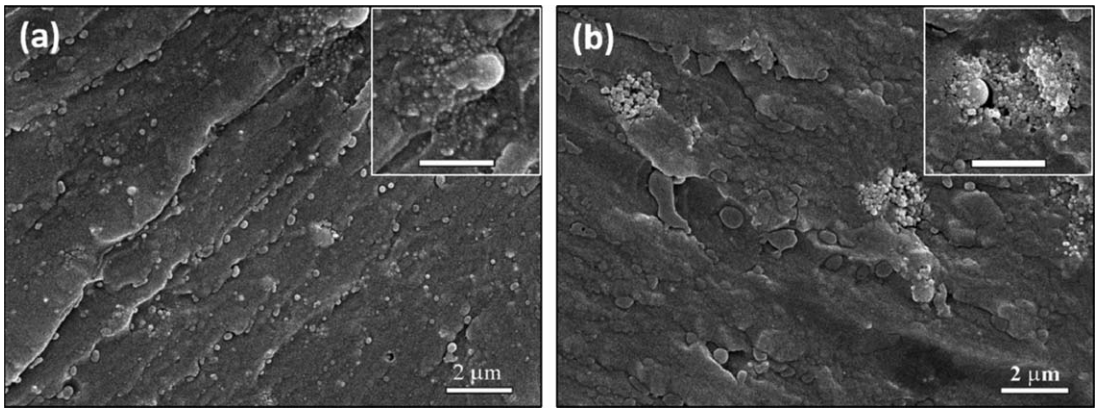

Figure 5. SEM images of the (a) nHAp and (b) nHAp@PEO nanocomposites. The insets highlight the nanoparticles. Scale bars of 2 μm.

In addition, the nHAp@PEO nanocomposite (Figure 7) presents well-defined nHAp agglomerates and smaller particles spread throughout the polymeric matrix. The carbon [Figure 7(b)] and calcium maps [Figure 7(c)] reveal that the small particles in Figure 7(a) also contain carbon and calcium, and they are probably particles consisting of nHAp and PEO. These observations suggest that the amount and length of the PEO block in the copolymer favor nHAp encapsulation.

The storage modulus (E'), loss modulus (E''), and tan δ versus temperature curves are shown in Figure 8. The analysis of the E' versus T curves reveals a continuous decrease from −75 to 100 °C from the initial storage modulus value of 3.10^9 to around 5.10^7 Pa, followed by an increment (to $1.5.10^8$ Pa) around 100 °C due to cold crystallization and by a decrease above 125 °C due to PLLA phase melting. The E'' versus T and tan δ versus T curves present two peaks up to 100 °C. The low temperature peak, at −45 °C, is more evident in the E'' versus T plot and it is attributed to the glass transition of the PEO phase. The peak at high temperature, at 60 °C, which is clear in the tan δ versus T plot, is attributed to the glass transition of the PLLA phase. Their maximum temperatures are assigned to the T_g of the PEO and PLLA phases (summarized in Table II).

The dynamic mechanical properties associated to PLLA-*b*-PEO-*b*-PLLA block copolymer relaxations have been previously described elsewhere.[28] The DMA results imply that the PLLA-*b*-PEO-*b*-PLLA copolymer and both nanocomposites are multiphase systems. E' decreases by one order of magnitude in the temperature range of the PEO glass transition, indicating that the copolymer presents a morphology of a PEO phase dispersed in a PLLA matrix.[28]

The glass transition of the PEO phase in the presence of the nHAp and nHAp@PEO nanofillers becomes narrower, as can be observed in the E'' versus T curves (Figure 8). This phenomenon is related to polymer/nanofiller specific interactions, which hinder the polymer chains relaxations. The mobility restriction and the free volume reduction of a polymer matrix due to the presence of hydroxyapatite particles have been reported for

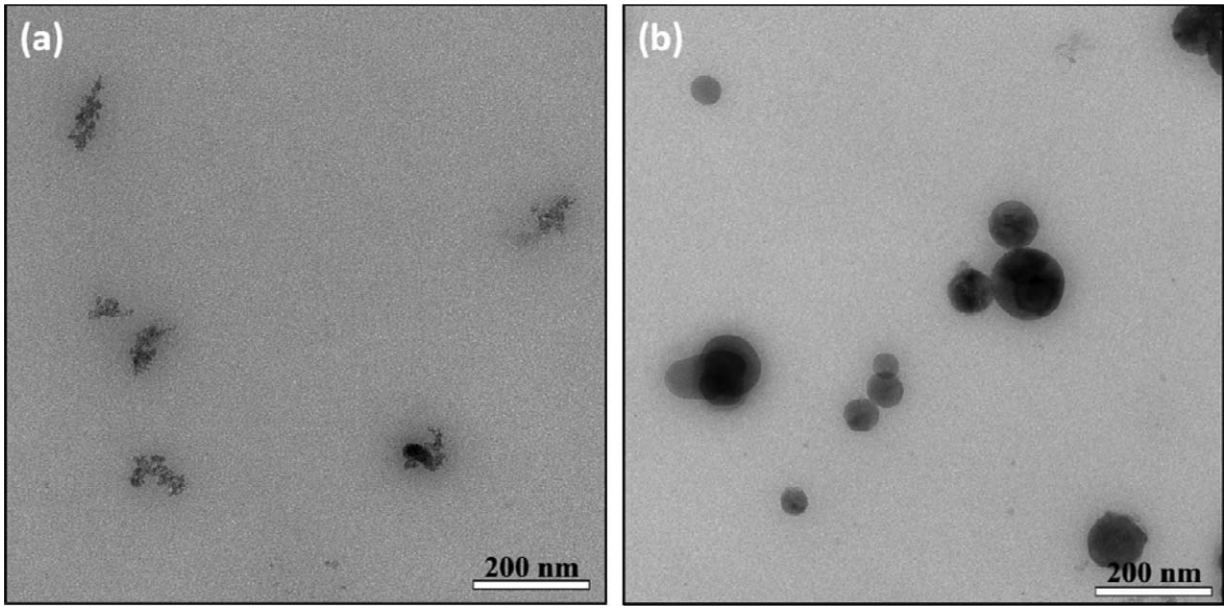

Figure 6. TEM bright field micrographs of the (a) PLLA-*b*-PEO-*b*-PLLA copolymer and (b) nHAp nanocomposite after processing.

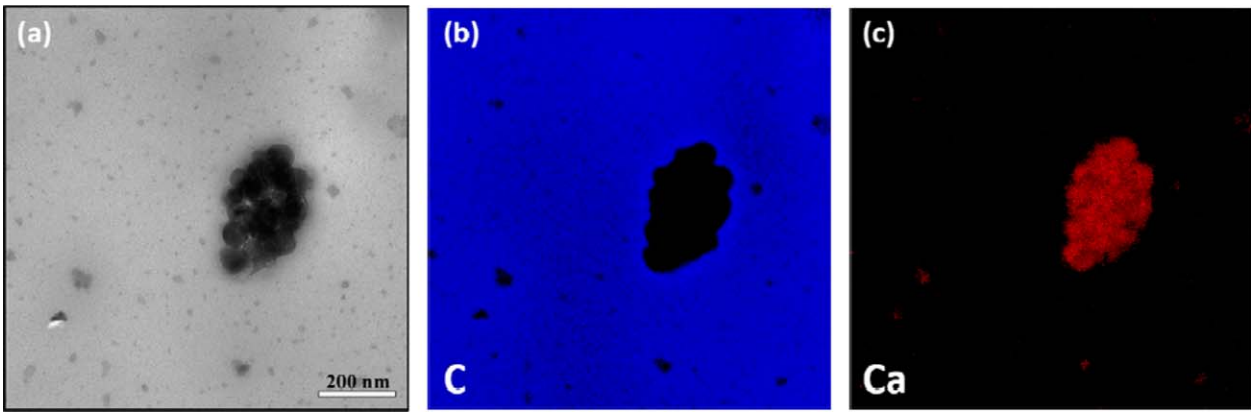

Figure 7. TEM bright field micrograph of the (a) nHAp@PEO nanocomposite and its (b) carbon and (c) calcium maps. [Color figure can be viewed in the online issue, which is available at wileyonlinelibrary.com.]

different polymers (for example: polylactide, polyethylene, polypropylene, polyamide) by many authors.[55–58] Moreover, the area of the peak in the tan δ versus T curves related to the glass transition of PLLA phase become higher with the addition of the nanofillers, meaning the increasing of the amorphous fraction and, consequently, of the relaxation capacity and energy conversion of the PLLA phase. This could be explained by the differences of the crystallinity degree of the PLLA phase in the copolymer and nanocomposites. Table II shows that the crystalline degree of PLLA phase increases in the inverse direction of the tan δ versus T area increment.

The main difference between copolymer and nanocomposites in E' versus T and E'' versus T curves are observed above PLLA phase glass transition at around 75–100 °C. At this temperature range, the storage and loss moduli of nHAp nanocomposite are smaller than the copolymer, due to the lower crystallinity degree of the PLLA phase.

The mechanical behavior of the nanocomposites was evaluated by means of nanoindentation experiments due to the reduced dimensions of the micro-injection moulded samples for evaluating the reinforcement effect of fillers in polymer-based nanocomposites.[59,60] The size of the deformed volume is larger than the morphological domains shown in Figure 5, and therefore, the measured curves are representative of the overall behavior of the nanocomposites.[61]

Figure 9(a) shows the typical indentation load-penetration depth curves obtained in depth sensing indentation experiments for all micro-injection moulded samples. Despite the higher crystallinity of PLLA blocks ($X_c = 49\%$, Table II) compared to neat $PLLA_{85}$ ($X_c = 28\%$), the copolymer behaves tougher and is more compliant than the $PLLA_{85}$. This indicates that the amorphous character of the PEO disperse phase in the copolymer overcomes the higher PLLA phase crystallinity degree, and it is, therefore, more relevant in determining the mechanical properties of the copolymer and nanocomposites. All samples showed hysteresis between loading and unloading stages and creep during the constant load stage. The impressions left of the sample surfaces are indicatives of plastic deformation and, consistent

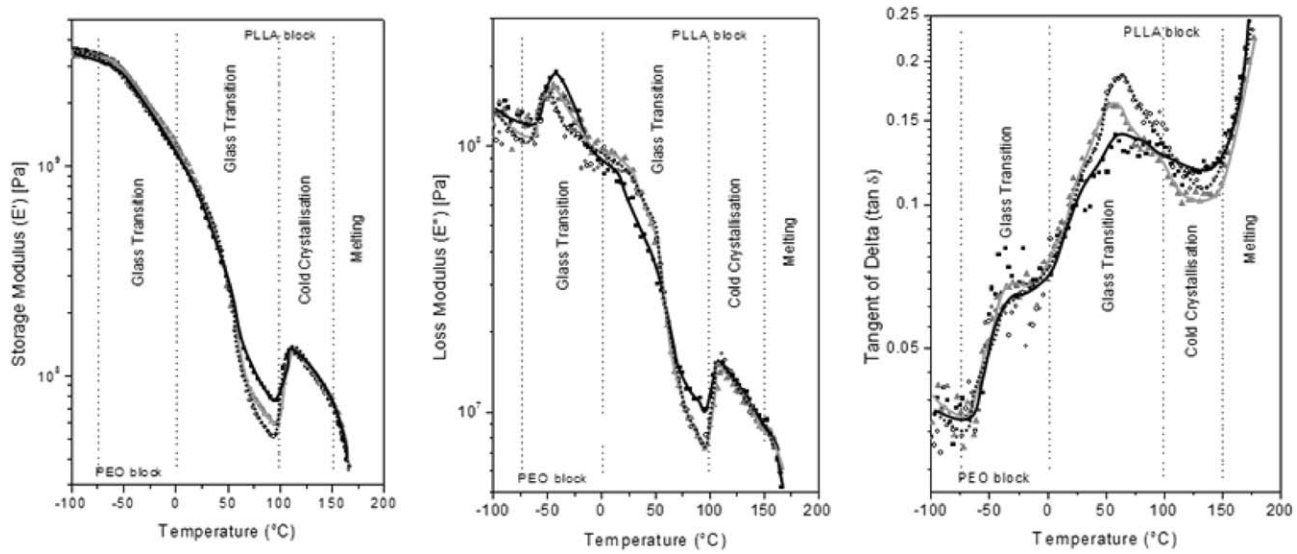

Figure 8. Storage (E') and loss (E'') moduli and tan δ versus temperature curves of (■) PLLA-*b*-PEO-*b*-PLLA, and of the (○) nHAp and (▲) nHAp@-PEO nanocomposites.

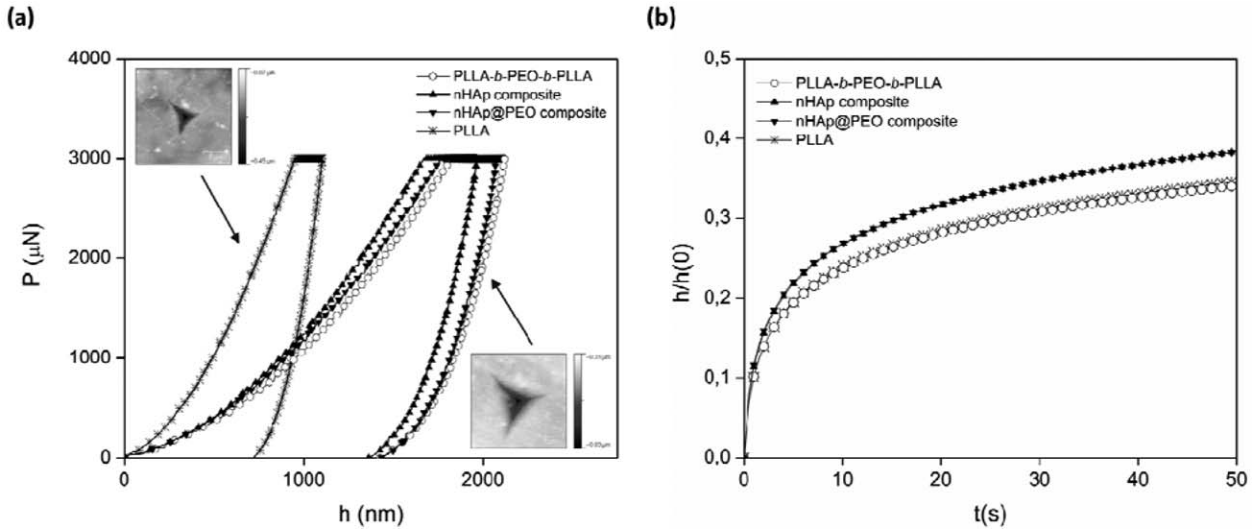

Figure 9. Nanoindentation experiments of the $PLLA_{85}$ homopolymer, copolymer and nanocomposites: (a) load penetration depth curves and (b) tip penetration depth measured as a function of time. The insets highlight the SPM images showing the impression left by the Berkovich indenter on the surfaces of the $PLLA_{85}$ and PLLA-*b*-PEO-*b*-PLLA samples.

with the shape of the load-penetration depth curves, the size of the impression left on the $PLLA_{85}$ surface by the Berkovich tip is smaller than that left on the PLLA-*b*-PEO-*b*-PLLA surface [the insets in Figure 9(a)].

The indentation curves of Figure 9(a) were analyzed following the Oliver-Pharr approach (see Supporting Information eq. S1) and the mechanical properties are given in Table II. It has been reviewed that E_r values of polymers and nanocomposites calculated by the Oliver-Pharr approach are generally in the range of those determined from conventional uniaxial tensile testing.[59] In addition, H values can be taken as a measure of the material yield stress as it is proportional to it.[62] The applied holding time at maximum load was enough to minimize the creep effects on the unloading curve. This condition was verified applying the post-experiment data correction proposed by Ngan *et al.*[63] For all samples, the difference between the corrected stiffness (S_c) and the one determined by the Oliver-Pharr method (S) was lesser than 1%.

The PLLA-*b*-PEO-*b*-PLLA copolymer displays lower E_r and H than the $PLLA_{85}$ homopolymer. The incorporation of nHAp and nHAP@PEO moderately increases the E_r and H of the pristine copolymer. No remarkable differences are observed in the mechanical properties of both nanocomposites. These results are in agreement with the storage modulus values reported at room temperature in Figure 8.

The slight improvement in the properties of the nanocomposites can be attributed to the balance between the polymer crystallinity and amount and dispersion of the stiff filler ($E \sim 80$ GPa for nHAp).[64] The crystallinity of PLLA achieved under the injection moulding conditions decreases with the incorporation of nHAp or nHAp@PEO, in comparison with that developed in the neat copolymer. Therefore, the expected large increment in properties due to the stiffening effect of the rigid nHAp and nHAp@PEO particles is partially compensated by the reduction in the matrix crystalline fraction. The lower degree of nanoparticle agglomeration observed in the nHAp nanocomposite sample, compared to the nHAp@PEO nanocomposite (Figure 5), may also contribute to the slightly higher increment in modulus. The partial agglomeration of nHAp@PEO nanoparticles leads to a lower adhesion to the matrix and to a reduction in the mechanical properties in comparison to nHAp nanocomposite. Similar results were reported for a biomimetic nanocomposite based on polyamide 6.9 (PA 6.9) and nHAp with load ratios ranging from 1 to 10 wt %.[58] The increment of storage modulus as a function of nHAp content in nanocomposites occurs until the limit value of 5 wt %. Above it, the storage modulus decreased, which was related to the decrease of the crystallinity degree and also to particle aggregation.[58]

Figure 9(b) shows the fractional increase in depth during the hold period of the indentation creep experiments. Creep model parameters, fitted according to eq. (S4) of Supporting Information, are given in Table II. The $PLLA_{85}$ semicrystalline homopolymer shows an inverse relationship between the strain rate sensitivity (A) and creep rate (B) parameters. This relationship has also been observed in other polymer systems.[40] The "instantaneous" penetration depth achieved at the end of the fast loading period, $h(0)$, is larger for PLLA-*b*-PEO-*b*-PLLA than for $PLLA_{85}$. However, the fractional increase in depth during the holding period of $PLLA_{85}$ and PLLA-*b*-PEO-*b*-PLLA practically coincided, meaning that the viscoelastic behavior of the copolymer is governed by the PLLA phase. The mechanism of deformation during indentation creep for a semicrystalline polymer is described as a "slippage" process in which the lamellar crystals slide within the viscous amorphous phase.[65] The addition of nHAp or nHAp@PEO resulted in the same and moderate increase in the strain rate sensitivity and creep rate, in comparison with the pristine copolymer creep behavior. The reduction of creep resistance can be attributed to the decrease in crystallinity degree in the nanocomposites, which prevails

over the expected inhibition of the "slippage" process imposed by the nanoparticles. Similar results were observed in other nanocomposite systems based on a semicrystalline matrix.[66]

CONCLUSIONS

Nanocomposites, combining the biocompatible triblock copolymer, PLLA-*b*-PEO-*b*-PLLA, and nHAp or PEO surface modified hydroxyapatite nanoparticles (nHAp@PEO), were successfully prepared by freeze-drying of benzene dispersions, followed by a micro-injection moulding process. The nanoparticles act as nucleating agents and nHAp@PEO is more efficient in increasing the crystallization temperature of PLLA and PEO blocks. The morphology of the PEO phase dispersed through the PLLA matrix for the copolymer is not affected by the presence of the nanofillers, and the mechanical properties of all the studied materials are governed by the PLLA phase. nHAp partially agglomerates after surface modification. However, both fillers are uniformly dispersed throughout the copolymer matrix. The injection moulded nanocomposites present lower crystallinity for the PLLA block phase, in comparison with the neat copolymer due to the processing conditions and also to the higher heat conductivity of the nanocomposites after nanofillers incorporation. The moderate increment of the elastic modulus E (~22%) and hardness H (~15%), while the creep resistance of the nanocomposites is reduced, in comparison to the neat PLLA-*b*-PEO-*b*-PLLA copolymer, is more pronounced for the nHAp nanocomposite and it reflects two opposing effects: the filler reinforcement and reduction in PLLA crystalline fraction. Our results indicate that the PEO blocks in the copolymer can disperse nHAp particles. Thus, we conclude that a previous encapsulation of the nHAp particles with PEO is not necessary to promote filler dispersion and improve mechanical properties. Compared to the reported conventional hydrophobic PLLA, the biocompatible PLLA-*b*-PEO-*b*-PLLA amphiphilic copolymer by itself exhibits advantages in dispersing hydrophilic nHAp and nHAp@PEO nanofillers with improved interfacial adhesion for bone tissue engineering applications.

ACKNOWLEDGMENTS

The authors would like to thank the São Paulo Research Foundation – FAPESP (processes number 2010/17804-7 and 2012/24821-0), Consejo Nacional de Investigaciones Científicas y Técnicas (CONICET), Conselho Nacional de Desenvolvimento Científico e Tecnológico – CNPq (process number 444392/2014-9) and Coordenação de Aperfeiçoamento de Pessoal de Nível Superior (Capes) for financial support.

REFERENCES

1. Gupta, B.; Revagade, N.; Hilborn, J. *Prog. Polym. Sci.* **2007**, *32*, 455.
2. Armentano, I.; Bitinis, N.; Fortunati, E.; Mattioli, S.; Rescignano, N.; Verdejo, R.; Lopez-Manchado, M. A.; Kenny, J. M. *Prog. Polym. Sci.* **2013**, *38*, 1720.
3. Sankaran, K. K.; Vasanthan, K. S.; Krishnan, U. M.; Sethuraman, S. *J. Tissue Eng. Regen. Med.* **2014**, *8*, 640.
4. Becker, J.; Lu, L.; Runge M. B.; Zeng, H.; Yaszemski, M. J.; Dadsetan, M. *J. Biomed. Mater. Res. Part A* **2015**, *103*, 2549.
5. Kumari, A.; Yadav, S. K.; Yadav, S. C. *Colloids Surf. B* **2010**, *75*, 1.
6. Jain, R. A. *Biomaterials* **2000**, *21*, 2475.
7. Kim, K.; Luu, Y. K.; Chang, C.; Fang, D.; Hsiao, B. S.; Chu, B.; Hadjiargyrou, M. *J. Control. Release* **2004**, *98*, 47.
8. Athanasiou, K. *Biomaterials* **1996**, *17*, 93.
9. Ciambelli, G. S.; Perez, M. O.; Siqueira, G. V.; Candella, M. A.; Motta, A. C.; Duarte, M. A. T.; Alberto-Rincon, M. C.; Duek, E. A. R. *Mater. Res.* **2013**, *16*, 28.
10. Middleton, J. C.; Tipton, A. J. *Biomaterials* **2000**, *21*, 2335.
11. Mäkelä, P.; Pohjonen, T.; Törmälä, P.; Waris, T.; Ashammakhi, N. *Biomaterials* **2002**, *23*, 2587.
12. Ghosh, S.; Viana, J. C.; Reis, R. L.; Mano, J. F. *Mater. Sci. Eng. C* **2008**, *28*, 80.
13. Nishizuka, T.; Kurahashi, T.; Hara, T.; Hirata, H.; Kasuga, T. *PLoS One* **2014**, *9*, e104603.
14. Torabinejad, B.; Mohammadi-Rovshandeh, J.; Davachi, S. M.; Zamanian, A. *Mater. Sci. Eng. C* **2014**, *42*, 199.
15. Kutikov, A. B.; Gurijala, A.; Song, J. *Tissue Eng. Part C Methods* **2015**, *21*, 229.
16. Medvecky, L. *Sci. World J.* **2012**, *2012*, 537973.
17. Fu, S. Z.; Meng, X. H.; Fan, J.; Yang, L. L.; Lin, S.; Wen, Q. L.; Wang, B. Q.; Chen L. L.; Wu J. B.; Chen, Y. *J. Biomed. Mater. Res. A* **2014**, *102*, 479.
18. Ji, J.; Dong, X. P.; Ma, X. H.; Tang, S. C.; Wu, Z. Y.; Xia, J.; Wang, Q. X.; Wang, Y.T.; Wei, J. *Appl. Surf. Sci.* **2014**, *317*, 1090.
19. Li, H.; Chang, J. *Compos. Sci. Technol.* **2005**, *65*, 2226.
20. Rajzer, I.; Menaszek, E.; Kwiatkowski, R.; Chrzanowski, W. *J. Mater. Sci. Mater. Med.* **2014**, *25*, 1239.
21. Diao, H.; Si, Y.; Zhu, A.; Ji, L.; Shi, H. *Mater. Sci. Eng. C* **2012**, *32*, 1796.
22. Liuyun, J.; Lixin, J.; Chengdong, X.; Lijuan, X.; Ye, L. *J. Biomater. Appl.* **2016**, *30*, 750.
23. Cheng, Z. Q.; Pang, G. H.; Wang, H. Y.; Li, J. F.; Zhao, X. Z. *Adv. Mater. Res.* **2012**, *535–537*, 1095.
24. Tudorachi, N.; Chiriac, A. P. *J. Polym. Environ.* **2011**, *19*, 546.
25. Yamini, D.; Devanand Venkatasubbu, G.; Kumar, J.; Ramakrishnan, V. *Spectrochim. Acta A* **2014**, *117*, 299.
26. Fu, S. Z.; Wang, X. H.; Guo, G.; Shi, S.; Fan, M.; Liang, H.; Luo, F.; Qian, Z. Y. *J. Biomed. Mater. Res. B* **2011**, *97*, 74.
27. Kutikov, A. B.; Song, J. *Acta Biomater.* **2013**, *9*, 8354.
28. Loiola, L. M. D.; Más, B. A.; Duek, E. A. R.; Felisberti, M. I. *Eur. Polym. J.* **2015**, *68*, 618.
29. Pielichowska, K., Blazewicz, S. *Adv. Polym. Sci.* **2010**, *232*, 97.
30. Ayatollahi, M. R.; Yahya, M. Y.; Asgharzadeh Shirazi, H.; Hassan, S. A. *Ceram. Int.* **2015**, *41*, 10818.
31. Trinca, R. B.; Felisberti, M. I. *J. Appl. Polym. Sci.* **2014**, *131*, DOI: 10.1002/app.40419.

32. Kricheldorf, H. R.; Meier-Haack, J. *Makromol. Chem.* **1993**, *194*, 715.
33. Wu, X.; El Ghzaoui, A.; Li, S. *Langmuir* **2011**, *27*, 8000.
34. Kimura, Y.; Matsuzaki, Y.; Yamane, H.; Kitao, T. *Polymer (Guildf)* **1989**, *30*, 1342.
35. Xiong, X. Y.; Li, Z. L.; Tam, K. C.; Li, Y. P.; Leng, J. Q.; Chen, H. Q.; Wang, Y. *J. Appl. Polym. Sci.* **2009**, *111*, 2445.
36. Rashkov, I.; Manolova, N.; Li, S. M.; Espartero, J. L.; Vert, M. *Macromolecules* **1996**, *29*, 50.
37. Scherrer, P. *Göttinger Nachr. Math. Phys.* **1918**, *2*, 98.
38. Holzwarth, U.; Gibson, N. *Nat. Nanotechnol.* **2011**, *6*, 534.
39. Oliver, W. C.; Pharr, G. M. *J. Mater. Res.* **1992**, *7*, 1564.
40. Beake, B. *J. Phys. D. Appl. Phys.* **2006**, *39*, 4478.
41. Tehrani, M.; Safdari, M.; Al-Haik, M. S. *Int. J. Plast.* **2011**, *27*, 887.
42. JCPDS File No. 9-432, International Center for Diffraction Data.
43. Lee, J. H.; Kim, I. T.; Tannenbaum, R.; Shofner, M. L. *J. Mater. Chem.* **2012**, *22*, 11556.
44. Irineu, J. A. F.; Marsi, T. C. O.; Santos, T. G.; Corat, E. J.; Marciano, F. R.; Lobo, A. O. *Mater. Lett.* **2012**, *79*, 166.
45. Panda, R. N.; Hsieh, M. F.; Chung, R. J.; Chin, T. S. *J. Phys. Chem. Solids* **2003**, *64*, 193.
46. Ma, J.; Wang, Y.; Zhou, L.; Zhang, S. *Mater. Sci. Eng. C* **2013**, *33*, 440.
47. Jiang, Y. M.; Li, X. H.; Feng, B.; Weng, J. *Key Eng. Mater.* **2005**, *284–286*, 55.
48. Younes, H.; Cohn, D. *J. Biomed. Mater. Res.* **1987**, *21*, 1301.
49. Fu, S.; Guo, G.; Gong, C.; Zeng, S.; Liang, H.; Luo, F.; Zhang, X.; Zhao, X.; Wei, Y.; Qian, Z. *J. Phys. Chem. B* **2009**, *113*, 16518.
50. Mark, J. E. Polymer Data Handbook. Journal of the American Chemical Society; Oxford University Press, Inc., New York, **1999**.
51. Kijima, T.; Tsutsumi, M. *J. Am. Ceram. Soc.* **1979**, *62*, 455.
52. Weidenfeller, B.; Höfer, M.; Schilling, F. R. *Compos. Part A* **2005**, *36*, 345.
53. Takahashi, S.; Imai, Y.; Kan, A.; Hotta, Y.; Ogawa, H. *J. Alloys Compd.* **2014**, *615*, 141.
54. Zhang, W.; Xu, X.; Yang, J.; Huang, T.; Zhang, N.; Wang, Y.; Zhou, Z. *Compos. Sci. Technol.* **2015**, *106*, 1.
55. Liu, X.; Wang, T.; Chow, L. C.; Yang, M.; Mitchell, J. W. *Int. J. Polym. Sci.* **2014**, *2014*, 8.
56. Alothman, O. Y.; Fouad, H.; Al-Zahrani, S. M.; Eshra, Y.; A.; Al Rez, M. F.; Ansari, S. G. *Biomed. Eng. Online* **2014**, *13*, 125.
57. Liu, Y.; Wang, M. *J. Appl. Polym. Sci.* **2007**, *106*, 2780.
58. Sender, C.; Dantras, E.; Dantras-Laffont, L.; Lacoste, M. H.; Dandurand, J.; Mauzac, M.; Lacout, J.-L.; Lavergne, C.; Demont, Ph.; Bernès, A.; Lacabanne, C. *J. Biomed. Mater. Res. Part B* **2007**, *83B*, 628.
59. Díez-Pascual, A. M.; Gómez-Fatou, M. A.; Ania, F.; Flores, A. *Prog. Mater. Sci.* **2015**, *67*, 1.
60. Gibson, R. F. *Compos. Sci. Technol.* **2014**, *105*, 51.
61. Fischer-Cripps, A. C. *Surf. Coatings Technol.* **2006**, *200*, 4153.
62. Fischer-Cripps, A. C. Introduction to Contact Mechanics; Springer-Verlag, New York, **2007**.
63. Ngan, A. H. W.; Wang, H. T.; Tang, B.; Sze, K. Y. *Int. J. Solids Struct.* **2005**, *42*, 1831.
64. Sharifi, S.; Kamali, M.; Mohtaram, N. K.; Shokrgozar, M. A.; Rabiee, S. M.; Atai, M.; Imani, M.; Mirzadeh, H. *Polym. Adv. Technol.* **2011**, *22*, 605.
65. Flores, A.; Ania, F.; Baltá-Calleja, F. J. *Polymer (Guildf)* **2009**, *50*, 729.
66. Shen, L.; Phang, I. Y.; Chen, L.; Liu, T.; Zeng, K. *Polymer (Guildf)* **2004**, *45*, 3341.